


Multigap superconductivity in lithium intercalated bilayer Mo₂C

Can Hong, Danhong Wu, Xi-Bo Li, and Feipeng Zheng *

College of Physics & Optoelectronic Engineering, Department of Physics, Jinan University, Guangzhou 510632, China



(Received 5 December 2023; accepted 7 February 2024; published 21 February 2024)

Interlayer coupling can significantly influence the physical properties of layered transition-metal compounds. The superconductivity in layered Mo₂C systems, belonging to the emergent family of MXene, has garnered considerable attention. However, the impact of interlayer coupling on superconductivity, and the anisotropic superconducting properties in these systems are not yet clear. By performing first-principles calculations of electron-phonon coupling and anisotropic superconducting properties, we show that the interlayer coupling in bilayer 1T-Mo₂C suppresses superconductivity, resulting in a significant drop in superconducting transition temperature (T_c) from 4.2 K in its monolayer form to nearly 0 K. By introducing lithium atoms into the interlayer space of the bilayer, the interlayer coupling can be effectively weakened, transforming the system into a two-gap superconductor with a T_c above 10 K. A 3% tensile strain can further transform the system into a three-gap superconductor with a significantly enhanced T_c of approximately 24.7 K, which is very high in the Mo₂C related systems. The enhancement of the superconductivity induced by the strain is mainly due to the downshift of an energy band with a flat dispersion to the energy near the Fermi level. The in-plane vibrations of Mo atoms and the d -orbital electrons of Mo atoms are most important for the formation of the superconductivity. Our method can also be applied to multilayer Mo₂C systems. Given the successful synthesis of layered Mo₂C systems and the experimental realization of alkaline-metal atom depositions, our work presents a practically feasible strategy for achieving high- T_c and multigap superconductivity in layered Mo₂C.

DOI: [10.1103/PhysRevB.109.064515](https://doi.org/10.1103/PhysRevB.109.064515)

I. INTRODUCTION

The interlayer coupling effect can vary across different layered systems. Take, for instance, the case of 2H-NbSe₂: the transition from a monolayer to a multilayer results in the enhancement of superconductivity while the weakening of the charge density wave [1]. In the case of 1T'-WTe₂, the transition from a monolayer to a multilayer structure results in an enhancement of its metallic properties, causing a decrease in the magnitude of the topological band gap from a positive to a negative value [2,3]. While in 1T-NiTe₂, superconductivity is suppressed on going from a monolayer to a bilayer [4]. Through interlayer coupling manipulation, their physical properties can be effectively tuned, leading to more diverse phases. For example, intercalating bulk 2H-NbSe₂ with cations allows it to retain its high superconducting transition temperature (T_c) while exhibiting the Ising superconductivity observed in its monolayer counterpart [5]. Incorporating hydrate molecules to decouple the interlayer of bulk 2H-NbSe₂ makes it nearly identical to the behaviors found in NbSe₂ monolayers with high charge density wave transition temperature and coexisting Ising superconductivity [6]. Intercalation of transition-metal atoms enables the change of charge order [7,8], introduction of magnetic order [9], and superconductivity [10]. Therefore, studying the interlayer coupling effects in layered compounds not only deepens the understanding of their physical properties, but also offers valuable insights for customizing these properties.

Transition-metal chalcogenides have garnered widespread attention due to their rich physical properties, such as the interplay between charge density waves and superconductivity, two-dimensional superconductivity, topologically nontrivial states, and magnetic order. More recently, the scope of investigation has extended to emergent transition-metal compounds, two-dimensional transition-metal nitrides, and carbonitrides, so-called MXenes. Among these, Mo₂C has received considerable interest, owing to its feasible synthesis, fascinating properties, and promising applications. Mo₂C can be crystalline in multistructure phases, among which orthorhombic α phase, and hexagonal H and T phases are of particular interest. They are experimentally feasible [11,12] and have been shown to be candidate materials for the study of the interplay between different orders due to the presence of superconductivity [11,13–24], the potential nonlinear Hall effect [23], and topological nontrivial states [13]. Among the above studies, extensive investigations have been conducted on the superconductivity of α -Mo₂C, encompassing both experimental and theoretical aspects. In detail, ultrathin α -Mo₂C has been synthesized and found to exhibit superconductivity with $T_c = 4$ K [11]. The superconductivity in this system has been observed to be weakened either with decreasing thickness [11], or in the regions near grain boundaries [16]. Further research indicates that the superconductivity is robust against defects [14]. Subsequent computational study reveals that the hardness of the superconducting α -Mo₂C is comparable to common alloys [18].

In contrast to the extensive experimental and theoretical investigations of superconductivity in α -Mo₂C, research on the superconductivity of layered H - and T -Mo₂C is currently

*Corresponding author: fpzheng_phy@email.jnu.edu.cn

predominantly on the theoretical aspect. Theoretical calculations reveal that monolayer $1T$ - Mo_2C and $1H$ - Mo_2C both exhibit superconductivity, with T_c approximately 5.9 K and 3.2 K, respectively [19,20]. Several approaches have been proposed to enhance their T_c s, including hydrogen adsorption [19,22], halogen atom adsorption [20], and biaxial strain [25]. Hydrogen adsorption on the surfaces of monolayer $1H$ - Mo_2C and $1T$ - Mo_2C leads to an increase in the T_c to approximately 12.6 K [19,21]. Additionally, Br atom adsorption enhances the T_c of monolayer $1T$ - Mo_2C to 12.8 K [20]. Applying a 4% tensile strain raises the T_c of monolayer $1T$ - Mo_2C to 6.7 K, while a 10% tensile strain increases the T_c of monolayer $1H$ - Mo_2C to 11.8 K [25]. Furthermore, a recent study suggests that the out-of-plane heterostructure formed by a monolayer $1T$ - Mo_2C and $1H$ - Mo_2C exhibits nonlinear Hall effects and potential Ising superconductivity [23]. However, there are several issues regarding the study of layered H and T phases of Mo_2C . First, the existing studies are mostly focused on monolayer systems. The superconductivity in their multilayer counterparts and the effect of interlayer coupling are unclear. Second, even when considering a small Coulomb repulsion in the calculations using Coulomb pseudopotential $\mu^* = 0.1$, the obtained T_c s were mostly below 13 K. Finally, the previous studies on the superconductivity were mostly using isotropic methods based on McMillan equation [26,27] except for the recent research on the heterostructure [23]. Thus, the anisotropic superconducting properties in layered Mo_2C , such as the distribution of the superconducting gap and its evolution with temperature, still need investigation, as these quantities are crucial for the understanding of superconductivity in low-dimensional systems with anisotropic Fermi surfaces [28–30].

In this study, we employed first-principles calculations to investigate the electronic structure, electron-phonon coupling, and anisotropic superconducting properties of few-layer Mo_2C , with a particular focus on bilayer configurations. We found that bilayer Mo_2C exhibits strong interlayer coupling, which acts to suppress its superconductivity, reducing the T_c from 4.2 K in its monolayer counterpart to 0 K. Interestingly, the introduction of lithium atoms into the interlayer space, serving to weaken the interlayer coupling through expanding interlayer space and simultaneously introducing electron doping, transforms the bilayer Mo_2C into a two-gap superconductor with a T_c exceeding 10 K, surpassing that of its monolayer counterpart. Remarkably, applying a small tensile strain of 3% significantly enhances superconductivity, transforming the system into a three-gap superconductor with a T_c of approximately 24.7 K, which is notably high compared to other layered Mo_2C -related systems. The methodologies applied here can also be extended to induce superconductivity in multilayer Mo_2C systems. Additionally, we will discuss the structure of superconducting gaps and the potential for Ising superconductivity in the system.

II. COMPUTATIONAL METHOD

Density-functional theory and density-functional perturbation theory calculations were performed using the PBE exchange-correlation functional [31], to scrutinize the crystal structures, electronic structures, and electron-phonon

coupling (EPC) of few-layer Mo_2C before and after the alkali-metal intercalations [32–34]. The crystal structures were visualized using VESTA package [35]. Nonlocal van der Waals interaction (vdw-df2-b86r) [36,37] was taken into account in the calculations of pristine multilayer Mo_2C . The projector augmented-wave pseudopotentials [38] were used to describe the interaction between the valence and core electrons. The Kohn-Sham valence states were expanded using plane waves, with energy cutoffs set at 50 Ry and 500 Ry for wave functions and charge densities, respectively. An $18 \times 18 \times 1$ \mathbf{k} mesh and a $6 \times 6 \times 1$ \mathbf{q} mesh were used to calculate the ground states of charge densities and phonons for bilayer systems, whereupon the EPC matrix elements, $g_{mn,\nu}(\mathbf{k}, \mathbf{q})$, were calculated [34]. The matrix elements quantify the scattering amplitude between the electronic states with a wave vector \mathbf{k} , a band index m [denoted as (\mathbf{k}, m)], and $(\mathbf{k} + \mathbf{q}, n)$ through a phonon mode with a branch ν and a wave vector \mathbf{q} . The above quantities were further interpolated [39] to a $120 \times 120 \times 1$ \mathbf{k} grid and a $60 \times 60 \times 1$ \mathbf{q} grid, whereby the Eliashberg function $\alpha^2F(\omega)$ was calculated. The Eliashberg function is defined as

$$\alpha^2F(\omega) = \frac{1}{2} \sum_{\nu} \int_{\text{BZ}} \frac{d\mathbf{q}}{\Omega_{\text{BZ}}} \omega_{q\nu} \lambda_{q\nu} \delta(\omega - \omega_{q\nu}),$$

where $\lambda_{q\nu}$ is a phonon-momentum-resolved EPC constant, Ω_{BZ} the volume of the first Brillouin zone. The Dirac delta function $\delta(\omega - \omega_{q\nu})$ is approximated by a Gaussian function with a broadening of 0.5 meV. The \mathbf{k} -resolved superconducting gaps on the Fermi surface at a temperature T , denoted as $\Delta(\mathbf{k}, T)$, were determined by solving the anisotropic Migdal-Eliashberg equations on an imaginary axis [28], and were subsequently analytically continued to a real axis with Padé functions. In solving the equations, the Kohn-Sham states within 100 meV around the Fermi level were included, and the Matsubara frequencies were cut off at 0.32 eV. The Coulomb pseudopotential μ^* used for the calculations of superconductivity, was estimated by $\mu^* \approx 0.26N(0)/[1 + N(0)]$, where $N(0)$ is the electronic density of states at the Fermi level [40].

III. RESULTS AND DISCUSSIONS

A. Physical properties of bilayer $1T$ - Mo_2C

We start by examining the crystal structure, electronic properties, and electron-phonon coupling in bilayer Mo_2C . Our calculations indicate that bilayer $1T$ - Mo_2C (hereinafter referred to as Mo_4C_2) exhibits the lowest total energy when compared to H and α phases (see Sec. S-I in the Supplemental Material [41]). The optimized hexagonal lattice constant for the Mo_4C_2 is 3.05 Å, slightly larger than that of its monolayer counterpart. The Mo_4C_2 is formed by the AA stacking of two $1T$ - Mo_2C monolayers, separated by a van der Waals (vdW) gap of approximately 2.25 Å, as illustrated in the inset of Fig. 1(b). In each monolayer, every carbon atom occupies the central position within an edge-shared octahedron, formed by six adjacent Mo atoms. This structure differs from that of transition-metal dichalcogenides in the same phase, where the transition-metal atoms occupy the center of the octahedron. The calculated phonon dispersion $[\omega(\mathbf{q})]$ depicted in Fig. 1(a) provides the evidence of the dynamical stability of

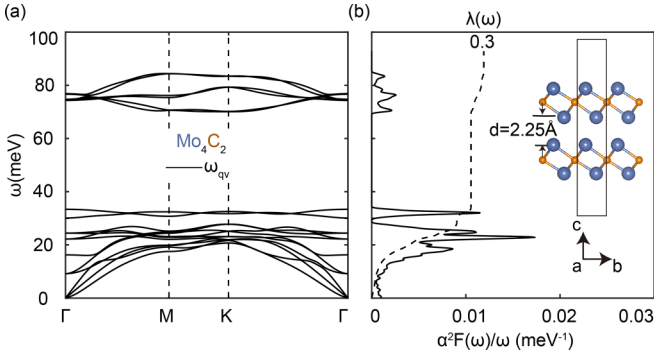


FIG. 1. (a) The phonon dispersion ω_{qv} , and (b) Eliashberg function $\alpha^2F(\omega)$ with the accumulated EPC constant $\lambda(\omega)$ of Mo_4C_2 . The inset in (b) shows the side view of the crystal structure of Mo_4C_2 . The black rectangle represents a unit cell.

Mo_4C_2 crystal, as it reveals the absence of any imaginary phonon modes. The calculated Eliashberg function [$\alpha^2F(\omega)$] and the integrated EPC [$\lambda(\omega)$] depicted in Fig. 1(b) show that the total EPC constant (λ) of the Mo_4C_2 is only 0.3. Using the Allen-Dynes-modified McMillan equation [26,27] with an estimated Coulomb pseudopotential $\mu^* = 0.157$, the superconducting T_c is estimated to be 0.0 K. In contrast, the calculated λ and T_c of monolayer $1T\text{-Mo}_2\text{C}$ are 0.76 and 4.2 K (Sec. S-II [41]), respectively, which are in line with a previous work [21]. This clearly demonstrates that EPC suppression occurs in the Mo_4C_2 compared to its monolayer counterpart, implying an adverse effect of interlayer coupling on the EPC. Additionally, the interlayer distance in Mo_4C_2 is only 2.25 Å according to our calculation, significantly smaller than that of commonly encountered transition-metal compounds like $2H\text{-NbSe}_2$ (2.94 Å) [42], bilayer $1T\text{-NiTe}_2$ (2.63 Å) [4], and bilayer $1T\text{-PtTe}_2$ (2.57 Å) [43], suggesting a strong interlayer coupling in the Mo_4C_2 . Indeed, our calculations, as shown in Sec. S-III [41], demonstrate that increasing the interlayer spacing in Mo_4C_2 effectively enhances $N(0)$, thereby providing additional electronic states for EPC. The impact of interlayer coupling on the $N(0)$ in Mo_4C_2 resembles that of NiTe_2 , and is in contrast to NbSe_2 and WTe_2 , where metallicity is reinforced in their multilayer counterparts. Alkaline-metal intercalation provides an effective method to relieve the interlayer coupling by expanding the interlayer space. By this method, the interlayer interaction was reduced in twisted bilayer MoS_2 , enabling fast Li-ion diffusion [44]. Furthermore, superconductivity can also be induced in group-IV honeycomb structures [45] and bilayer transition-metal dichalcogenides [4,43]. Thus, it is expected that such method can be applied to Mo_4C_2 .

B. Method for preparing lithium intercalated Mo_4C_2

Our findings suggest that it is energetically unfavorable to directly insert alkaline-metal atoms into the interlayer space of Mo_4C_2 , primarily due to strong interlayer coupling (see Sec. S-IV [41]). Alternatively, we identified an energetically favorable method to create alkali-metal intercalated Mo_4C_2 , consisting of two steps as illustrated in Fig. 2. First, lithium atoms were deposited onto the surface of a monolayer

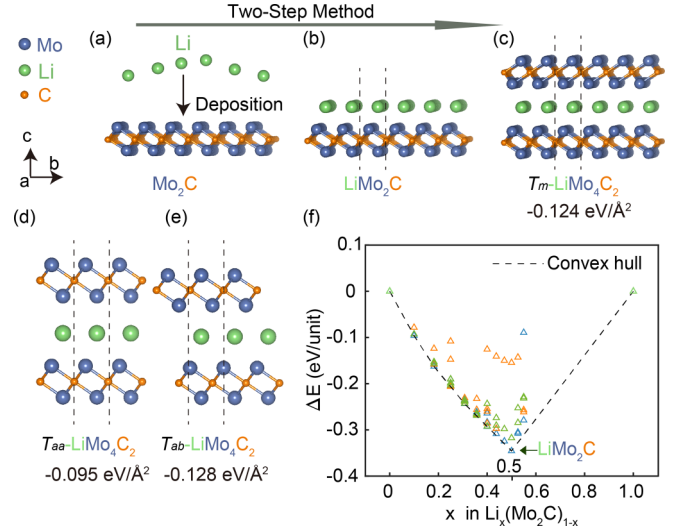


FIG. 2. The proposed two-step process for preparing LiMo_4C_2 . First, lithium atoms are deposited on a monolayer $1T\text{-Mo}_2\text{C}$ surface as shown in (a) and (b). The corresponding formation energies as a function of lithium concentrations (x) are presented in (f), along with a convex Hull (see main text for details). The blue, orange, and green triangles represent the formation energies of the configurations where the lithium atoms sit above the bottom Mo atoms, top Mo atoms, and C atoms, respectively (see Sec. S-V [41] for more details). Second, the LiMo_2C is further covered by a monolayer Mo_2C to form LiMo_4C_2 . Three configurations of LiMo_4C_2 with formation energies of -0.124 , -0.095 , and -0.128 $\text{eV}/\text{\AA}^2$ are displayed in (c)–(e), respectively.

$1T\text{-Mo}_2\text{C}$. The chemical formula for a unit of the lithium-adsorbed monolayer Mo_2C can be denoted as $\text{Li}_m(\text{Mo}_2\text{C})_n$, where m and n are integer numbers. Alternatively, it can be expressed as $\text{Li}_x(\text{Mo}_2\text{C})_{1-x}$, with $x = m/(m+n)$ denoting the lithium concentration. To investigate the thermally stable compositions of $\text{Li}_x(\text{Mo}_2\text{C})_{1-x}$, we calculated the formation energies as a function of the x , defined as $\Delta E(x) = E[\text{Li}_x(\text{Mo}_2\text{C})_{1-x}] - xE[\text{Li}] - (1-x)E[\text{Mo}_2\text{C}]$, where $E[\text{Li}]$ and $E[\text{Mo}_2\text{C}]$ represent the energies of a body-centered cubic lithium crystal per atom and a monolayer $1T\text{-Mo}_2\text{C}$ crystal per Mo_2C , respectively. There are three distinct adsorption sites on the $1T\text{-Mo}_2\text{C}$ monolayer surface where lithium atoms can bind, including the sites above the carbon atoms, the sites above the top-layer Mo atoms, and the sites above the bottom-layer Mo atoms [see Figs. S4(b) and S4(d) [41]]. The computed results, depicted in Fig. 2(f), reveal that when all sites above the bottom-layer Mo atoms are occupied (corresponding to $x = 0.5$), the resultant LiMo_2C [$\text{Li}_{0.5}(\text{Mo}_2\text{C})_{0.5}$] configuration on [Fig. 2(b)] exhibits the most negative formation energy and resides on the convex hull, as indicated by the blue triangle at $x = 0.5$. When additional Li atoms are deposited ($x > 0.5$) and the structures are optimized, the resulting formation energies start to increase, deviating from the convex hull, as illustrated in Fig. 2(f). These findings underscore the thermal stability of the LiMo_2C with the lithium atoms adsorbed above the bottom Mo atoms, indicating its resistance to decomposition into other compounds with different stoichiometries. The phonon dispersion calculation shown in Fig. S5 [41] further confirms the dynamical stability of the

LiMo₂C. We also considered the deposition of lithium on a monolayer 1*H*-Mo₂C. However, we found that there can be a phase transition from 1*H* to 1*T* when lithium atoms adsorb on the monolayer 1*H*-Mo₂C surface, reminiscent of the same phase transition in layered MoS₂ induced by Li interaction [44] (see Sec. S-V [41]).

After analyzing the Li depositions, we found that a monolayer Mo₂C is energetically favorable to cover the Li adlayer, forming the Li intercalated bilayer LiMo₂C with a stoichiometry of LiMo₄C₂. We identified three different configurations with the same stoichiometry of LiMo₄C₂, but with different stacking orders of the two internal monolayers. For the *T_m*-LiMo₄C₂, as illustrated in Fig. 2(c), the two monolayers are related by a horizontal mirror symmetry across the Li adlayer. In the *T_{aa}*-LiMo₄C₂ configuration, as shown in Fig. 2(d), the two monolayers are AA stacked. For the *T_{ab}*-LiMo₄C₂, as depicted in Fig. 2(e), the two monolayers stack in the order similar to the case of graphite. By calculating their formation energies defined as $(E[\text{LiMo}_4\text{C}_2] - E[\text{LiMo}_2\text{C}] - E[\text{Mo}_2\text{C}])/S$, where the *S* donates an area of a two-dimensional unit cell for the LiMo₂C, we found that the *T_m*, *T_{ab}*, and *T_{aa}* phases have the formation energies of -0.124 , -0.128 , and -0.095 eV/Å², respectively, as labeled in Figs. 2(c)–2(e). The above results suggest that the *T_m*-LiMo₄C₂ and *T_{ab}*-LiMo₄C₂ have relatively low formation energies and are energetically more favorable to be synthesized. The dynamical stabilities of *T_m*-LiMo₄C₂ and *T_{ab}*-LiMo₄C₂ were also confirmed by the phonon calculations as displayed in Figs. 4(a) and S9(a) [41], respectively. Given the relative lower formation energies of *T_m*-LiMo₄C₂ and *T_{ab}*-LiMo₄C₂, and the more significant EPC enhancement in *T_m*-LiMo₄C₂, which we will show below, our focus will be on the *T_m*-LiMo₄C₂ in the main text.

C. Electronic structure of *T_m*-LiMo₄C₂

We anticipate that the weakening of interlayer coupling in *T_m*-LiMo₄C₂ will increase $N(0)$, as we have previously analyzed. Figure 3(a) illustrates the electronic band structure of *T_m*-LiMo₄C₂, demonstrating its metallic nature. Several bands cross the Fermi level, resulting in electron and hole Fermi pockets, as indicated by black circles in Figs. 3(e) and 3(f). There is a pair of conduction bands across the Fermi level, with a slight energy splitting attributed to weak interlayer coupling. Their band minima along the *k*-path of Γ -*K* are approximately -0.1 eV below the Fermi level, while those along Γ -*M* are slightly above it. This results in six electronic pockets near Γ , as depicted in Figs. 3(e) and 3(f). By projecting the electronic states near the Fermi level onto atomic orbitals, as shown in Figs. 3(e) and 3(f), it is evident that the electronic states around these six pockets are primarily derived from the Mo-*d* orbitals. Furthermore, a valence band, mainly derived from the Mo-*d* with slight admixtures of Mo-*p* and Mo-*s* orbitals, intersects the Fermi level around the *M* points, with its band maximum approximately 0.13 eV above Fermi level [Fig. 3(a)]. This leads to a hole pocket centered at *M* [Figs. 3(e)–3(f)]. The multiband Fermi surface of *T_m*-LiMo₄C₂ leads to a calculated $N(0) = 3.87$ states/eV/Mo₂C, which is more than twice as large as that of Mo₄C₂. This finding is consistent with the calculated

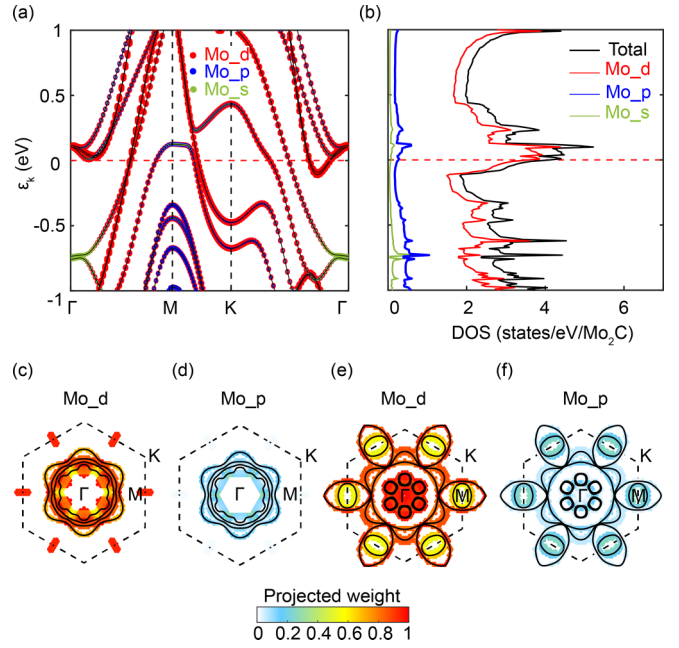


FIG. 3. (a) The projected electronic band structure, (b) density of states, and (e)–(f) Fermi surface onto the atomic orbitals of Mo atoms for *T_m*-LiMo₄C₂. (c)–(d) The projected Fermi surface onto the atomic orbitals of Mo atoms for Mo₄C₂. In (c)–(f), the Fermi surfaces are represented by solid black curves, while the boundaries of the corresponding Brillouin zones are indicated by dashed lines.

Fermi surface of Mo₄C₂, as shown in Figs. 3(c) and 3(d), where the electronic states near the Fermi level are clearly fewer compared with those in *T_m*-LiMo₄C₂.

D. Enhanced electron-phonon coupling in *T_m*-LiMo₄C₂

The increase of $N(0)$ leads to the increase of EPC in *T_m*-LiMo₄C₂. The calculated λ of *T_m*-LiMo₄C₂ is 0.85, which is nearly triple the value of Mo₄C₂, as shown in Fig. 4(b). By comparing the Eliashberg functions $\alpha^2F(\omega)$ of the above two materials, it is clear that the promotion of λ in *T_m*-LiMo₄C₂ is primarily attributed to the phonon energy in the region between 0 and 25 meV, where intensive peaks [Fig. 4(b)], and large phonon-momentum-resolved EPC constant ($\lambda_{q\nu}$) [Fig. 4(a)] can be observed. More specifically, the $\lambda(\omega = 25$ meV) of *T_m*-LiMo₄C₂ is 0.66, exhibiting a 247% increase compared to the value of Mo₄C₂ (0.19). By decomposing the $\alpha^2F(\omega)$ into the contributions of the different atomic vibrations, we can quantitatively reveal the origin of the EPC enhancement. The decomposition can be performed using the following equation [43]:

$$\alpha^2F(\omega, j, \hat{n}) = \frac{1}{2} \sum_{\nu} \int_{\text{BZ}} \frac{d\mathbf{q}}{\Omega_{\text{BZ}}} \omega_{\mathbf{q}\nu} \lambda_{\mathbf{q}\nu} \delta(\omega - \omega_{\mathbf{q}\nu}) |\hat{n} \cdot \mathbf{e}_{\mathbf{q},\nu}^j|^2,$$

where $\mathbf{e}_{\mathbf{q},\nu}^j$ is the component of the atom *j* in the polarization vector related to $\omega_{\mathbf{q}\nu}$, and \hat{n} is the unit projection direction vector, pointing to the in-plane (*xy*) or out-of-plane (*z*) direction. The integration of $\alpha^2F(\omega, j, \hat{n})$ leads to the atomic-vibration-resolved EPC constant $\lambda(j, \hat{n})$ as illustrated in Fig. 4(d). Comparing the calculated $\lambda(j, \hat{n})$ of *T_m*-LiMo₄C₂ and Mo₄C₂, it is evident that the $\lambda(j, \hat{n})$ exhibits an overall

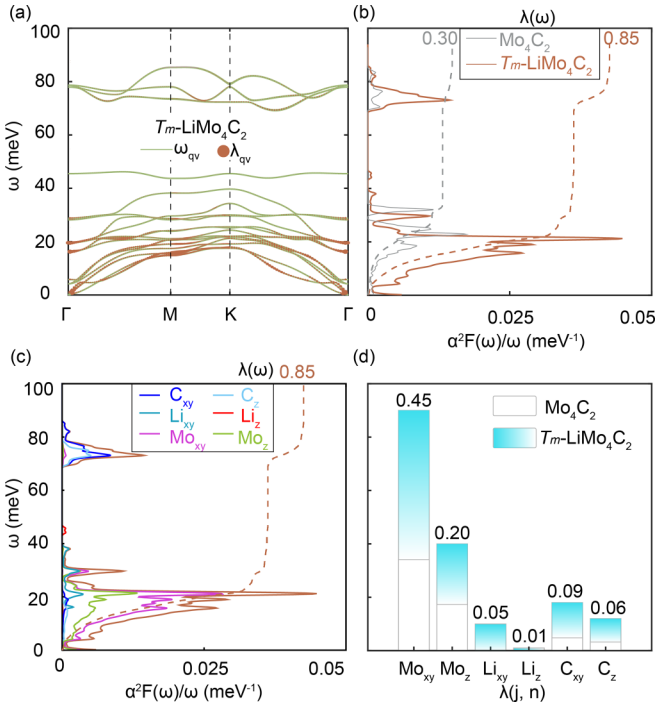


FIG. 4. (a) Phonon dispersion ($\omega_{q\nu}$) along with phonon-momentum-resolved EPC constant ($\lambda_{q\nu}$) for T_m -LiMo₄C₂. (b) Eliashberg spectra divided by phonon energy [$\alpha^2 F(\omega)/\omega$] along with accumulated EPC constant [$\lambda(\omega)$] for T_m -LiMo₄C₂ and Mo₄C₂. (c) Projected $\alpha^2 F(\omega)/\omega$ onto in-plane (xy) and out-of-plane (z) vibrations of each atom in T_m -LiMo₄C₂. (d) Atomic-vibration-resolved EPC constant for T_m -LiMo₄C₂, obtained by integrating the corresponding spectra in (c). The results of Mo₄C₂ are also shown for comparison.

enhancement in T_m -LiMo₄C₂. Notably, the contributions from the in-plane and out-of-plane vibrations of Mo atoms (Mo- xy and Mo- z) increase by 153% and 121%, respectively, reaching 0.45 and 0.20. The enhancements of EPC related to Mo- xy and Mo- z vibrations are evident in the $\alpha^2 F(\omega, j, \hat{n})$ depicted in Fig. 4(c), where the peaks associated with Mo- xy and Mo- z are observed within the energy range of 0–25 meV. The above discussion indicates that the significant EPC enhancement in T_m -LiMo₄C₂ arises from the contributions of low-energy phonons associated with Mo vibrations.

E. Two-gap superconductivity in T_m -LiMo₄C₂

The enhancement of EPC strength and the presence of a multiband Fermi surface result in two-gap superconductivity with an enhanced superconducting T_c in T_m -LiMo₄C₂, as demonstrated below. We employ the imaginary-time anisotropic Migdal-Eliashberg formalism, followed by analytic continuation to the real axis using Padé functions, through which the \mathbf{k} -resolved superconducting gaps at Fermi surface under finite temperature, $\Delta(\mathbf{k}, T)$, can be obtained. In solving the anisotropic Migdal-Eliashberg equations, the estimated $\mu^* = 0.208$ based on $N(0)$ is used (see Sec. II for details). The histogram in Fig. 5(a) illustrates the temperature-dependent variation in the energy distribution of $\Delta(\mathbf{k}, T)$. It is evident that the magnitude of $\Delta(\mathbf{k}, T)$ decreases as the

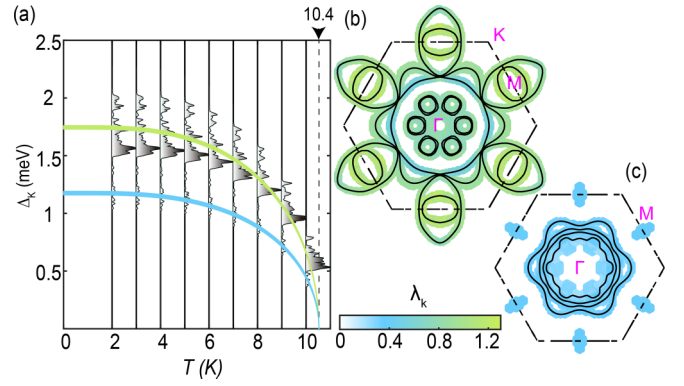


FIG. 5. (a) Histograms of $\Delta(\mathbf{k}, T)$ for T_m -LiMo₄C₂ at various temperatures. The green and blue curves are the BCS fits of the two gaps. Distribution of \mathbf{k} -resolved EPC constants near Fermi surface for (b) T_m -LiMo₄C₂ and (c) Mo₄C₂. In (b) and (c), the Fermi surfaces are represented by solid black curves, while the boundaries of the corresponding Brillouin zones are indicated by dashed lines.

temperature increases. The $\Delta(\mathbf{k}, T)$ eventually reaches zero at $T = 10.4$ K, indicating that the calculated T_c for T_m -LiMo₄C₂ is 10.4 K. Moreover, upon analyzing the structure of $\Delta(\mathbf{k}, T)$, it is evident that the system exhibits a two-gap characteristic. At a given temperature, most of the \mathbf{k} states exhibit a higher magnitude of $\Delta(\mathbf{k}, T)$, while the remaining states display a lower magnitude. For instance, at $T = 2$ K, the majority of \mathbf{k} states exhibit the values of $\Delta(\mathbf{k}, T)$ ranging from about 1.5–2.0 meV, while the remaining \mathbf{k} states fall within the range of approximately 1.0–1.4 meV. This can be also confirmed from the distribution of $\Delta(\mathbf{k}, T = 2$ K) in the Brillouin zone, as shown in Fig. S7(b) [41]. The two-gap characteristic is consistent with the distributions of the \mathbf{k} -resolved EPC constant $\lambda_{\mathbf{k}}$ shown in Fig. 5(b), where the \mathbf{k} states around the large circular Fermi pocket at Γ have lower $\lambda_{\mathbf{k}}$ values of around 0.4, whereas the other \mathbf{k} states have higher $\lambda_{\mathbf{k}}$ values close to 1.0. The aforementioned circular Fermi pocket indicates isotropic characteristics, resembling the behavior of a free electron gas system. The enhanced EPC in T_m -LiMo₄C₂ compared to Mo₄C₂ is also evident by comparing Figs. 5(b) and 5(c), where the $\lambda_{\mathbf{k}}$ of T_m -LiMo₄C₂ [Fig. 5(b)] shows an overall increase.

F. Three-gap superconductivity with high T_c in T_m -LiMo₄C₂ induced by a small tensile strain

Given possible in-plane strains in ultrathin materials, which can be induced by a substrate, the potential discrepancies in lattice constants between PBE calculations and experimental measurements, and the significance contribution to the EPC of T_m -LiMo₄C₂ from Mo_{xy} vibration, it is necessary to investigate the evolution of EPC and superconductivity in response to in-plane strains for this material. We apply biaxial strains to T_m -LiMo₄C₂ by adjusting the in-plane lattice constant and then optimizing its internal coordinates. We define a biaxial strain as $(a - a_0)/a_0$, where $a_0 = 3.01$ Å is the optimized hexagonal lattice constant of T_m -LiMo₄C₂ without strains, and a is the lattice constant under strains. In Fig. 6(a), the evolutions of $N(0)$ and λ with strains are depicted. It is evident that both $N(0)$ and λ increase with the tensile

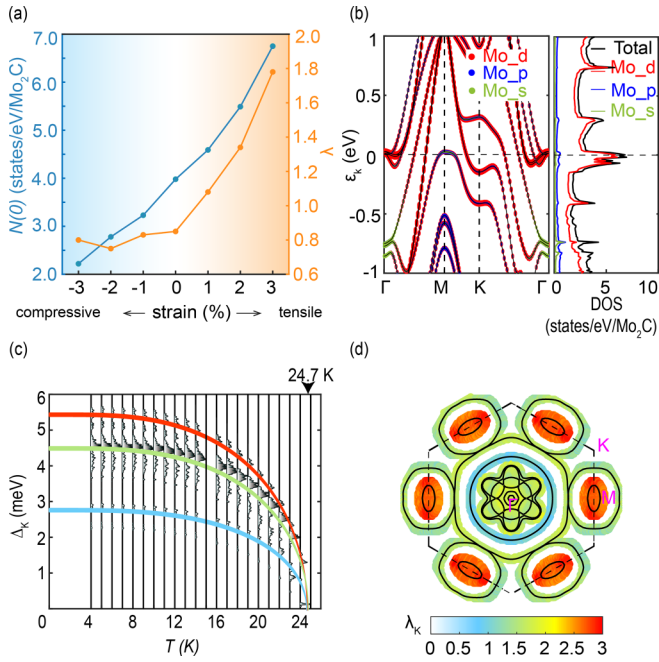


FIG. 6. (a) Evolution of $N(0)$ and λ as a function of strains for T_m -LiMo₄C₂. (b) Projected band structure and DOS onto the atomic orbitals for T_m -LiMo₄C₂ under a 3% tensile strain. (c) Histograms of $\Delta(\mathbf{k}, T)$, and (d) the distribution of λ_k near Fermi surface for the T_m -LiMo₄C₂ under a 3% tensile strain. In (d), the Fermi surface is represented by solid black curves, while the boundary of the Brillouin zone is indicated by dashed lines.

strain, peaking at 3% strain with values of approximately 6.8 states/eV/Mo₂C and 1.78, respectively. It is evident from Fig. 7(a) that the crystal structure of T_m -LiMo₄C₂ under the 3% strain is dynamically stable. Further increase the tensile strain leads to the dynamical instability of the T_m -LiMo₄C₂ crystal. The rise in $N(0)$ under the 3% tensile strain can be understood by comparing the band structure and Fermi surface with strain [Figs. 6(b) and 6(d)] to those without strain [Figs. 3(a) and 5(b)]. The most significant change in the band structure after applying the strain is the downward shift of the valence band top near the M points, as evident when comparing Fig. 6(b) with Fig. 3(a). Since the valence band curvature is relatively flat near its top, this downward shift clearly increases number of the states near the Fermi level. This is seen by comparing the DOS depicted in Fig. 3(b) and 6(b), where the peak at 0.13 eV [Fig. 3(b)] has shifted downward to an energy very close to the Fermi level [Fig. 6(b)], in accordance with the shift of the valence band top. Furthermore, the conduction bands, with their bottoms located near Γ , also undergo downward shifts. This results in the merging of six Fermi circles near Γ into larger circles centered at Γ , accompanied by the appearance of additional small Fermi circles around Γ . These alterations in the band structure contribute significantly to the increased value of $N(0)$. This, in turn, provides a greater number of scattering channels and electronic states available for EPC, which are responsible for the substantial enhancement of λ from 0.85–1.78 [Fig. 7(b)]. The superconductivity in T_m -LiMo₄C₂ is expected to be strengthened due to the increased λ . The $\Delta(\mathbf{k}, T)$ of the strained T_m -LiMo₄C₂ was

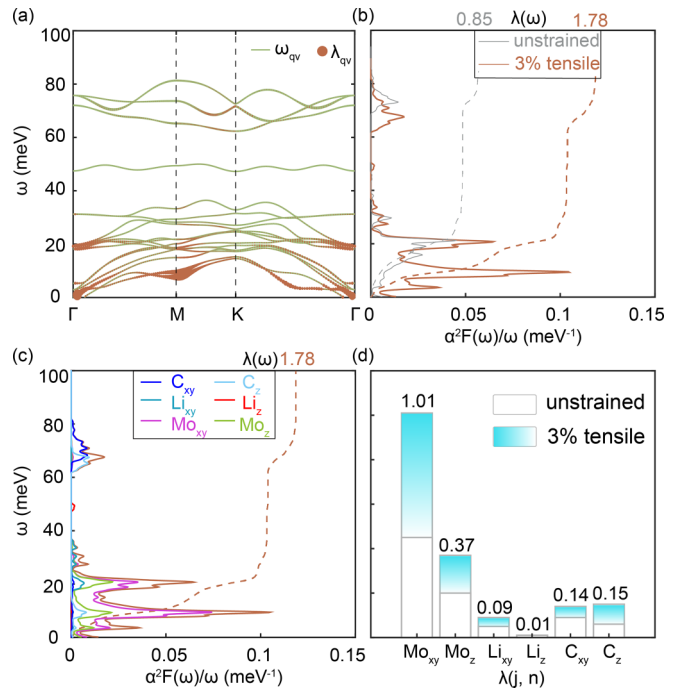


FIG. 7. (a) The ω_{qv} of T_m -LiMo₄C₂ under a 3% tensile strain, along with the corresponding λ_{qv} . (b) The $\alpha^2F(\omega)/\omega$ along with $\lambda(\omega)$ for the T_m -LiMo₄C₂ with and without the tensile strain. (c) Projected $\alpha^2F(\omega)/\omega$ onto in-plane (xy) and out-of-plane (z) vibrations of each atom in the tensile strained T_m -LiMo₄C₂. (d) Atomic-vibration-resolved EPC constant for the tensile strained T_m -LiMo₄C₂, obtained by integrating the corresponding spectra in (c). The results of the unstrained T_m -LiMo₄C₂ are also shown for comparison.

calculated based on the aforementioned anisotropic Migdal-Eliashberg formalism, with an estimated $\mu^* = 0.226$. The evolution of the $\Delta(\mathbf{k}, T)$ histogram, as depicted in Fig. 6(c), clearly indicates that the T_c for T_m -LiMo₄C₂ under 3% tensile strain is 24.7 K, more than twice the T_c in the strain-free case (10.4 K). Interestingly, a transition from a two-gap superconductor to a three-gap superconductor is clearly discernible when examining the structure of the $\Delta(\mathbf{k}, T)$ histogram at temperatures below T_c , as illustrated in Fig. 6(c). For example, at $T = 4$ K, the $\Delta(\mathbf{k}, T)$ histogram exhibits three primary peaks centered at approximately 5.4, 4.5, and 2.8 meV, respectively. The distributions of λ_k , as shown in Fig. 6(d), indicate that the \mathbf{k} states with relatively large $\Delta(\mathbf{k})$ around 5.4 meV are located around the M points in the Brillouin zone. The \mathbf{k} states with relatively small $\Delta(\mathbf{k})$ around 2.8 meV primarily originate from the circular Fermi circles centered at Γ , akin to the strain-free case discussed previously. The remaining \mathbf{k} states, as shown in Fig. 6(d), exhibit a moderate magnitude of $\Delta(\mathbf{k})$ around 4.5 meV. By comparing the $\Delta(\mathbf{k}, T)$ distributions shown in Figs. 5(b) and 6(d), it is clear that the transition of the state from the two gaps to the three gaps is primarily due to the presence of the \mathbf{k} states with large λ_k values near the M points. These emergent \mathbf{k} states originate from the valence band top near the Fermi level, characterized by a notably flat dispersion, as previously mentioned. The significant variation of λ_k for the \mathbf{k} states near different Fermi pockets strongly implies an anisotropic Fermi surface. This underscores the

significance of accounting for the anisotropic behavior of $\Delta(\mathbf{k}, T)$ when calculating the superconducting properties of the system.

To further elucidate the mechanism of the strain effect on the EPC, we present the $\alpha^2F(\omega)$ plots for both the unstrained and 3% tensile-strained T_m -LiMo₄C₂ in Fig. 7(b). It is evident that the increase in EPC after the strain primarily stems from the enhancement of EPC in the low-energy phonon range, approximately 0–25 meV. More specifically, the deviation of $\lambda(\omega = 25 \text{ meV})$ between these two cases is 0.82, accounting for nearly 88% of the discrepancy in their λ values (0.93). Examining the $\alpha^2F(\omega, j, \hat{n})$ plot presented in Fig. 7(c) clarifies that the rise in λ within the low-energy range mainly results from the enhanced EPC associated with Mo_{xy}. This is evident because the $\alpha^2F(\omega, \text{Mo}, xy)$ within the energy range of 0–25 meV closely matches the $\alpha^2F(\omega)$. The computed $\lambda(\text{Mo}, xy)$ values for T_m -LiMo₄C₂, before and after the 3% tensile strain, as depicted in Fig. 7(d), provide further support for this observation. As the $\lambda(\text{Mo}, xy)$ value increases substantially by approximately 125%, rising from 0.45–1.01.

The T_{ab} -LiMo₄C₂ exhibits analogous properties to T_m -LiMo₄C₂. The unstrained T_{ab} -LiMo₄C₂ was calculated to be a two-gap superconductor with a T_c of 11.2 K [Fig. S6(a) [41]], slightly higher than that of T_m -LiMo₄C₂. More details can be found in Sec. S-VII [41]. Under a 3% tensile strain, T_{ab} -LiMo₄C₂ undergoes a similar transition to T_m -LiMo₄C₂, shifting from a two-gap superconductor to a three-gap one with a T_c of 18.9 K [Fig. S11(a) [41]], slightly lower than that of T_m -LiMo₄C₂. More details can be found in Sec. S-VIII [41].

We note that the T_{ab} -LiMo₄C₂ crystal carries inversion symmetry, with inversion centers positioned at the lithium atom sites. In contrast, the T_m -LiMo₄C₂ crystal lacks inversion symmetry. Noncentrosymmetric two-dimensional superconductors have the potential to host Ising superconductivity, in which their magnitude of upper critical magnetic fields exceed far beyond the Pauli limits due to locking of spins along the out-of-plane direction, stemming from strong spin-orbit coupling. Recently, it was theoretically predicted that the out-of-plane heterojunction formed by monolayer 1H-Mo₂C and 1T-Mo₂C could be an Ising superconductor with a spin-orbit splitting magnitude comparable to that of the gated MoS₂ [23], a classic Ising superconductor [46]. In contrast to the heterojunction, our calculations for the noncentrosymmetric T_m -LiMo₄C₂ suggest that spin-orbit coupling has a minimal impact on the Fermi surface (see Sec. S-IX [41]), indicating that T_m -LiMo₄C₂ is unlikely to host Ising superconductivity.

In addition to the lithium atoms, we have also explored the utilization of other alkali-metal atoms for the intercalation, including sodium, potassium, and rubidium atoms. We found that only the sodium atoms are energetically favorable to adsorb on the monolayer Mo₂C surface. The formation energies are also negative when another monolayer Mo₂C is covered onto the sodium adlayer to form NaMo₄C₂. This suggests that the sodium intercalated bilayer Mo₂C can also be prepared (Sec. S-X [41]).

Furthermore, in Sec. S-XI [41], we show that the lithium intercalations can also increase the $N(0)$ in multilayer Mo₂C including trilayer, four-layer, and bulk Mo₂C. The extents of

$N(0)$ enhancements due to lithium intercalation in the trilayer, four-layer, and bulk Mo₂C are similar to that observed in the bilayer, as discussed above. This suggests that superconductivity can also be induced by lithium intercalation in multilayer Mo₂C other than the bilayer.

IV. CONCLUSION

In summary, we have computationally studied the crystal structure, electronic structure, phonon, EPC, and superconductivity in bilayer Mo₂C and related systems. We find that strong interlayer coupling diminishes the $N(0)$ of bilayer 1T-Mo₂C, subsequently reducing the superconducting T_c from 4.2 K in its monolayer counterpart to 0 K. A two-step method, involving the deposition of lithium atoms and subsequent covered with a Mo₂C monolayer, enables the intercalation of lithium atoms, resulting in the formation of T_m -LiMo₄C₂ and T_{ab} -LiMo₄C₂ crystals. The insertion of lithium atoms not only increases the interlayer spacing of the bilayer system, weakening the interlayer coupling, but also introduces electron doping. These combined effects significantly enhance the $N(0)$ and the EPC in the LiMo₄C₂ systems. By computing the anisotropic superconducting properties, we find that both T_m -LiMo₄C₂ and T_{ab} -LiMo₄C₂ systems exhibit two-gap superconductivity, with T_c s of 10.2 and 11.2 K, respectively. The vibrational modes of Mo atoms and the anisotropic EPC of the electronic states near the Fermi surface, particularly involving the d -orbital states of Mo atoms, play dominant roles in the formation of the two-gap superconductivity. A 3% biaxial tensile strain can further induce a transition from two-gap to three-gap superconductivity in T_m -LiMo₄C₂, with a significantly enhanced T_c of 24.7 K. This transition is primarily attributed to the downward shift of a flat dispersion near M points to the vicinity of the Fermi level, which not only enhances the $N(0)$, but also brings in the \mathbf{k} states with exceptionally strong EPC strengths. From the perspective of atomic vibrations, the substantial enhancement of EPC due to the in-plane vibrations of Mo atoms plays a crucial role in this superconducting transition. Meanwhile, the 3% biaxial tensile strain can also induce a three-gap superconductivity in T_{ab} -LiMo₄C₂, raising the T_c to 18.9 K. The methods described in this work can be possibly applied to multilayer Mo₂C systems. Considering that layered Mo₂C systems have been successfully synthesized [12], and the depositions of alkaline-metal atoms can also be realized experimentally [47,48], our work provides an experimentally feasible strategy for achieving multigap superconductivity with high transition temperatures in layered Mo₂C systems.

ACKNOWLEDGMENTS

This work is supported by National Natural Science Foundation of China 11804118, Guangdong Basic and Applied Basic Research Foundation (Grant No. 2021A1515010041), and the Science and Technology Planning Project of Guangzhou (Grant No. 202201010222). The calculations were performed on high-performance computation cluster of Jinan University, and Tianhe Supercomputer System.

- [1] X. Xi, L. Zhao, Z. Wang, H. Berger, L. Forró, J. Shan, and K. F. Mak, *Nat. Nanotechnol.* **10**, 765 (2015).
- [2] X. Qian, J. Liu, L. Fu, and J. Li, *Science* **346**, 1344 (2014).
- [3] F. Zheng, C. Cai, S. Ge, X. Zhang, X. Liu, H. Lu, Y. Zhang, J. Qiu, T. Taniguchi, K. Watanabe, S. Jia, J. Qi, J.-H. Chen, D. Sun, and J. Feng, *Adv. Mater.* **28**, 4845 (2016).
- [4] F. Zheng, X.-B. Li, P. Tan, Y. Lin, L. Xiong, X. Chen, and J. Feng, *Phys. Rev. B* **101**, 100505(R) (2020).
- [5] H. Zhang, A. Rousuli, K. Zhang, L. Luo, C. Guo, X. Cong, Z. Lin, C. Bao, H. Zhang, S. Xu, R. Feng, S. Shen, K. Zhao, W. Yao, Y. Wu, S. Ji, X. Chen, P. Tan, Q. K. Xue, Y. Xu *et al.*, *Nat. Phys.* **18**, 1425 (2022).
- [6] R. Sun, J. Deng, X. Wu, M. Hao, K. Ma, Y. Ma, C. Zhao, D. Meng, X. Ji, and Y. Ding, *Nat. Commun.* **14**, 6689 (2023).
- [7] S. Wu, R. Basak, W. Li, J.-W. Kim, P. J. Ryan, D. Lu, M. Hashimoto, C. Nelson, R. Acevedo-Estevés, S. C. Haley, J. G. Analytis, Y. He, A. Frano, and R. J. Birgeneau, *Phys. Rev. Lett.* **131**, 186701 (2023).
- [8] T. Luo, M. Zhang, J. Shi, and F. Zheng, *Phys. Rev. B* **107**, L161401 (2023).
- [9] Y. Huan, T. Luo, X. Han, J. Ge, F. Cui, L. Zhu, J. Hu, F. Zheng, X. Zhao, L. Wang, J. Wang, and Y. Zhang, *Adv. Mater.* **35**, 2207276 (2023).
- [10] S. Pan, M. Hong, L. Zhu, W. Quan, Z. Zhang, Y. Huan, P. Yang, F. Cui, F. Zhou, J. Hu, F. Zheng, and Y. Zhang, *ACS Nano* **16**, 11444 (2022).
- [11] C. Xu, L. Wang, Z. Liu, L. Chen, J. Guo, N. Kang, X.-L. Ma, H.-M. Cheng, and W. Ren, *Nat. Mater.* **14**, 1135 (2015).
- [12] X. Zhao, W. Sun, D. Geng, W. Fu, J. Dan, Y. Xie, P. R. Kent, W. Zhou, S. J. Pennycook, and K. P. Loh, *Adv. Mater.* **31**, 1808343 (2019).
- [13] N.-N. Zhao, P.-J. Guo, X.-Q. Lu, Q. Han, K. Liu, and Z.-Y. Lu, *Phys. Rev. B* **101**, 195144 (2020).
- [14] Z. Zhang, H. Gedeon, Z. Cheng, C. Xu, Z. Shao, H. Sun, S. Li, Y. Cao, X. Zhang, and Q. Bian, *Nano Lett.* **19**, 3327 (2019).
- [15] Y. Fan, C. Xu, X. Liu, C. Ma, Y. Yin, H.-M. Cheng, W. Ren, and X. Li, *NPG Asia Mater.* **12**, 60 (2020).
- [16] Z. Liu, C. Xu, C. Wang, S. Song, L. Wang, Y. Wang, N. Kang, X. Ma, H.-M. Cheng, and W. Ren, *Nano Lett.* **19**, 857 (2019).
- [17] J. Zhang, Z. Cao, X. He, W. Liu, Y. Wen, L. Cavallo, W. Ren, H. Cheng, and X. Zhang, *J. Phys. Chem. Lett.* **12**, 2219 (2021).
- [18] Y. Ge, H. Song, K. Bao, S. Ma, L. Li, Q. Tao, P. Zhu, B. Liu, D. Duan, and T. Cui, *J. Alloys Compd.* **881**, 160631 (2021).
- [19] J. Lei, A. Kutana, and B. I. Yakobson, *J. Mater. Chem. C* **5**, 3438 (2017).
- [20] J.-J. Zhang and S. Dong, *J. Chem. Phys.* **146**, 034705 (2017).
- [21] J. Bekaert, C. Sevik, and M. V. Milošević, *Nanoscale* **12**, 17354 (2020).
- [22] J. Bekaert, C. Sevik, and M. V. Milošević, *Nanoscale* **14**, 9918 (2022).
- [23] N.-N. Zhao, Z.-F. Ouyang, P.-H. Sun, J.-F. Zhang, K. Liu, and Z.-Y. Lu, *Phys. Rev. B* **108**, 035140 (2023).
- [24] L. Wang, C. Xu, Z. Liu, Z. Liu, Z. Yang, H. Cheng, W. Ren, and N. Kang, *Adv. Elec. Mater.* **9**, 2201170 (2023).
- [25] H.-D. Liu, H.-Y. Lu, N. Jiao, M.-M. Zheng, Y.-P. Li, L. Yang, B.-T. Wang, and P. Zhang, *Phys. Chem. Chem. Phys.* **25**, 580 (2022).
- [26] W. L. McMillan, *Phys. Rev.* **167**, 331 (1968).
- [27] P. B. Allen and R. C. Dynes, *Phys. Rev. B* **12**, 905 (1975).
- [28] E. R. Margine and F. Giustino, *Phys. Rev. B* **87**, 024505 (2013).
- [29] H. J. Choi, D. Roundy, H. Sun, M. L. Cohen, and S. G. Louie, *Nature (London)* **418**, 758 (2002).
- [30] A. Sanna, S. Pittalis, J. K. Dewhurst, M. Monni, S. Sharma, G. Umrigar, S. Massidda, and E. K. U. Gross, *Phys. Rev. B* **85**, 184514 (2012).
- [31] J. P. Perdew, K. Burke, and M. Ernzerhof, *Phys. Rev. Lett.* **77**, 3865 (1996).
- [32] G. Kresse and J. Furthmüller, *Phys. Rev. B* **54**, 11169 (1996).
- [33] P. Giannozzi, S. Baroni, N. Bonini, M. Calandra, R. Car, C. Cavazzoni, D. Ceresoli, G. L. Chiarotti, M. Cococcioni, I. Dabo, A. Dal Corso, S. de Gironcoli, S. Fabris, G. Fratesi, R. Gebauer, U. Gerstmann, C. Gougousis, A. Kokalj, M. Lazzeri, L. Martin-Samos *et al.*, *J. Phys.: Condens. Matter* **21**, 395502 (2009).
- [34] S. Poncé, E. R. Margine, C. Verdi, and F. Giustino, *Comput. Phys. Commun.* **209**, 116 (2016).
- [35] K. Momma and F. Izumi, *J. Appl. Cryst.* **44**, 1272 (2011).
- [36] I. Hamada, *Phys. Rev. B* **89**, 121103(R) (2014).
- [37] K. Lee, É. D. Murray, L. Kong, B. I. Lundqvist, and D. C. Langreth, *Phys. Rev. B* **82**, 081101(R) (2010).
- [38] G. Kresse and D. Joubert, *Phys. Rev. B* **59**, 1758 (1999).
- [39] A. A. Mostofi, J. R. Yates, Y.-S. Lee, I. Souza, D. Vanderbilt, and N. Marzari, *Comput. Phys. Commun.* **178**, 685 (2008).
- [40] K. H. Bennemann and J. W. Garland, in *AIP Conf. Proc.*, Vol. 4 (AIP, College Park, 1972), pp. 103–137.
- [41] See Supplemental Material at <http://link.aps.org/supplemental/10.1103/PhysRevB.109.064515> for calculated properties for monolayer and bilayer 1T-MoC₂, monolayer 1T-LiMo₂C, and T_{ab}-LiMo₄C₂.
- [42] M. Marezio, P. D. Dernier, A. Menth, and G. W. Hull Jr, *J. Solid State Chem.* **4**, 425 (1972).
- [43] D. Wu, Y. Lin, L. Xiong, J. Li, T. Luo, D. Chen, and F. Zheng, *Phys. Rev. B* **103**, 224502 (2021).
- [44] Y. Wu, J. Wang, Y. Li, J. Zhou, B. Y. Wang, A. Yang, L.-W. Wang, H. Y. Hwang, and Y. Cui, *Nat. Commun.* **13**, 3008 (2022).
- [45] J. A. Flores-Livas and A. Sanna, *Phys. Rev. B* **91**, 054508 (2015).
- [46] Y. Saito, Y. Nakamura, M. S. Bahrany, Y. Kohama, J. Ye, Y. Kasahara, Y. Nakagawa, M. Onga, M. Tokunaga, T. Nojima *et al.*, *Nat. Phys.* **12**, 144 (2016).
- [47] T. Jaouen, A. Pulkkinen, M. Rumo, G. Kremer, B. Salzmann, C. W. Nicholson, M. L. Mottas, E. Giannini, S. Tricot, P. Schieffer, B. Hildebrand, and C. Monney, *Phys. Rev. Lett.* **130**, 226401 (2023).
- [48] P. Rosenzweig, H. Karakachian, D. Marchenko, K. Küster, and U. Starke, *Phys. Rev. Lett.* **125**, 176403 (2020).